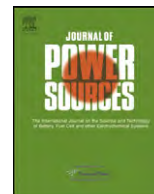




Contents lists available at ScienceDirect

Journal of Power Sources

journal homepage: [www.elsevier.com/locate/jpowsour](http://www.elsevier.com/locate/jpowsour)

## Pd-substituted (La,Sr)CrO<sub>3-δ</sub>-Ce<sub>0.9</sub>Gd<sub>0.1</sub>O<sub>2-δ</sub> solid oxide fuel cell anodes exhibiting regenerative behavior

David M. Bierschenk<sup>a</sup>, Elizabeth Potter-Nelson<sup>a</sup>, Cathleen Hoel<sup>b</sup>, Yougui Liao<sup>a</sup>, Laurence Marks<sup>a</sup>, Kenneth R. Poeppelmeier<sup>b</sup>, Scott A. Barnett<sup>a,\*</sup>

<sup>a</sup> Department of Materials Science and Engineering, Northwestern University, 2220 Campus Dr., Evanston, IL 60208, USA

<sup>b</sup> Department of Chemistry, Northwestern University, Evanston, IL 60208, USA

### ARTICLE INFO

#### Article history:

Received 22 November 2010  
Received in revised form 8 December 2010  
Accepted 10 December 2010  
Available online 21 December 2010

#### Keywords:

SOFC  
Oxide anode  
Palladium  
Perovskite  
Catalyst

### ABSTRACT

Composite anodes consisting of Pd-substituted (La,Sr)CrO<sub>3-δ</sub> mixed with 50 wt% Ce<sub>0.9</sub>Gd<sub>0.1</sub>O<sub>2-δ</sub> were tested in La<sub>0.9</sub>Sr<sub>0.1</sub>Ga<sub>0.8</sub>Mg<sub>0.2</sub>O<sub>3-δ</sub>-electrolyte supported fuel cells at 800 °C with humidified H<sub>2</sub> fuel. Low anode polarization resistance was observed during the first several hours of operation, explained by the nucleation of Pd nano-particles on perovskite particle surfaces. Anode performance then degraded gradually before stabilizing. Redox cycling repeatedly restored the anodes to their initial peak performance, followed again by degradation. This regenerative behavior was explained by the observation that the Pd nano-particles were removed by oxidation, and then re-nucleated upon reduction.

© 2010 Published by Elsevier B.V.

### 1. Introduction

Oxide anodes have received significant attention as possible alternatives to Ni-cermet anodes in solid oxide fuel cells (SOFCs) [1]. While reasonably low polarization resistance ( $R_p$ ) has been reported for a few oxide materials [2–4],  $R_p$  can be improved by adding nano-scale precious metal catalysts to the anodes. This has been achieved either by wet impregnation and calcination [5,6] or by incorporating the catalyst element directly into the perovskite prior to anode fabrication [7–10]. In the latter method, termed here “catalyst precipitation”, electro-catalytic nano-particles form on oxide particle surfaces upon exposure to fuel [8]. For example, La<sub>0.8</sub>Sr<sub>0.2</sub>Cr<sub>0.82</sub>Ru<sub>0.18</sub>O<sub>3-δ</sub> anodes form Ru nano-particles that reduce anode polarization by ~65% [7].

An advantage of catalyst precipitation is that a high density of very small (down to ~1 nm) [9] particles are formed, maximizing their electro-catalytic effect such that substantial performance enhancements result from cost-effective amounts of precious metal.<sup>1</sup> However, the small size also has a disadvantage, as there is a

strong driving force for coarsening of nano-particles that degrades their electro-catalytic effect [10]. For the Ru-substituted chromite case noted above, the coarsening resulted in a slight increase in polarization resistance over 300 h at 800 °C. A possible solution is to periodically re-dissolve the nano-particles into the oxide phase, and then re-precipitate them in their small and highly active state. There is a precedent for this in automotive catalysts, where repeated precipitation and dissolution of precious-metal nano-particles has been reported for precious-metal-substituted perovskite catalyst materials exposed to redox cycles [11,12]. However, attempts to regenerate the Ru-substituted chromite anodes, by redox cycling after Ru nano-particles had formed, were unsuccessful [8].

Here we report a new SOFC anode material, Pd-substituted (La,Sr)CrO<sub>3-δ</sub>. Pd incorporated into the perovskite phase resulting in the formation of Pd nano-particles upon exposure to fuel and helped yield relatively low  $R_p$  values. Compared to the Ru-substituted chromite, the Pd-substituted anode evolved more rapidly but anodes stabilized at a similar  $R_p$  after >300 h of operation [9,10,13]. Regeneration of the initial low  $R_p$  was observed after redox cycling the Pd-substituted anodes, where the Pd nano-particles disappeared upon oxidation and re-precipitated upon subsequent reduction.

### 2. Experimental

The anode powders were prepared by mixing appropriate quantities of La<sub>2</sub>O<sub>3</sub>, SrCO<sub>3</sub>, Cr<sub>2</sub>O<sub>3</sub>, and PdO. The amounts

\* Corresponding author. Tel.: +1 847 491 2447; fax: +1 847 491 7820.

E-mail address: [s-barnett@northwestern.edu](mailto:s-barnett@northwestern.edu) (S.A. Barnett).

<sup>1</sup> Although Pd is a precious metal, the amount used is quite small such that the cost is not prohibitive. In particular, for the present composition and anode dimensions, the Pd loading is ~0.3 mg pe cm<sup>2</sup> of anode. This assumes a density of 6.6 g cm<sup>-3</sup> for the LSCrPd, that the volume fraction of LSCrPd is 33%, and a functional layer thickness of 15 μm. For a Pd price of 600 USD per oz, this corresponds to a Pd cost of ~15> USD kW<sup>-1</sup>.

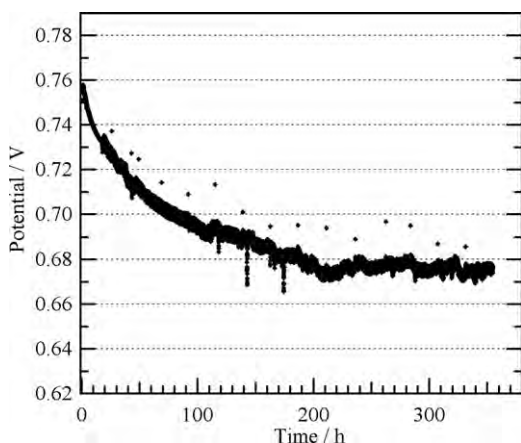


Fig. 1. LSCrPd–GDC cell voltage versus time at 800 °C and  $J = 600 \text{ mA cm}^{-2}$ .

were chosen aiming to produce the nominal compositions  $\text{La}_{0.8}\text{Sr}_{0.2}\text{Cr}_{0.8}\text{Pd}_{0.2}\text{O}_{3-\delta}$  (LSCrPd),  $\text{La}_{0.8}\text{Sr}_{0.2}\text{Cr}_{0.95}\text{Pd}_{0.05}\text{O}_{3-\delta}$  (LSCrPd05), and  $\text{La}_{0.8}\text{Sr}_{0.2}\text{CrO}_{3-\delta}$  (LSCr), if the product was a homogeneous single phase. The precursors were mixed with wet ball milling in ethanol for 24 h. The PdO was obtained by heating  $\text{PdO}\cdot x\text{H}_2\text{O}$  (Alfa Aesar) at 800 °C for 1 h. The milled slurries were dried and calcined at 1200 °C for 3 h. The observed LSCrPd and LSCrPd05 products were primarily perovskite, but also contained secondary Pd-rich phases as described below. Thus, the perovskite phase had less Pd than planned.

$\text{La}_{0.9}\text{Sr}_{0.1}\text{Ga}_{0.8}\text{Mg}_{0.2}\text{O}_{3-\delta}$  (LSGM) electrolyte pellets were prepared by solid-state reaction from oxides or carbonates, dry pressing, and firing at 1450 °C as described elsewhere [7]. All cathode and anode layers were prepared by screen printing electrode inks onto the LSGM pellets. Inks were prepared by first wet ball milling in ethanol the relevant powder(s), following by drying, sieving, and suspending in a vehicle (Heraeus, V-737) using a three roll mill. The anode active layers were  $\text{La}_{0.8}\text{Sr}_{0.2}\text{Cr}_{1-x}\text{Pd}_x\text{O}_{3-\delta}\text{-Ce}_{0.9}\text{Gd}_{0.1}\text{O}_{2-\delta}$  (GDC) composites (1:1 weight ratio), with LSCr current collectors; these layers were co-fired at 1200 °C for 3 h. The cathode active layers were  $\text{La}_{0.6}\text{Sr}_{0.4}\text{Fe}_{0.8}\text{Co}_{0.2}\text{O}_{3-\delta}$  (LSCF, Praxair)–GDC (NexTech) composites (1:1 wt ratio), with LSCF current collectors; the layers were co-fired at 1000 °C for 3 h. The resulting cell electrode areas were  $0.5 \text{ cm}^2$  and defined the active area of the cells. A gold (Heraeus C5756) current collector grid was then screen printed on both electrodes.

Button cell tests were carried out on cells sealed to alumina tubes with Ag ink (DAD-87, Shanghi Research Insitute of Synthetic Resins) [8]. Anodes were heated and tested in 50 sccm humidified

$\text{H}_2$  (97%  $\text{H}_2$ /3%  $\text{H}_2\text{O}$ ) and the cathodes were open to stagnant lab air. Electrochemical impedance spectroscopy (EIS) was done at open circuit using a 20 mV AC signal from  $10^6 \text{ Hz}$  to 0.1 Hz with a Zahner IM-6 electrochemical workstation. The cell  $R_p$  was determined by fitting the data with Z-View. The cells were fit with three cole elements in series with an inductor and a resistor. Life tests were recorded using a Keithley Instruments 2420 source meter.

Anode redox cycles were performed at the open circuit condition. Each redox cycle consisted of an Ar purge (<5 min), exposure to airflow at 50 sccm (variable time), another Ar purge, and then exposure to 50 sccm humidified  $\text{H}_2$ . During redox cycles, the cell was maintained at 800 °C and the voltage was recorded.

Powder X-ray diffraction (XRD) patterns were collected on a Rigaku D/MAX X-ray diffractometer using Cu  $\kappa\alpha 1$  radiation and analyzed with Jade 8.0 (Materials Data Inc.). Scanning electron microscopy was completed on a Hitachi S4800-II. Transmission electron microscopy (TEM) and scanning transmission electron microscopy (STEM) with energy dispersive X-ray spectroscopy (EDS) analysis was completed on a JEOL JEM-2100F.

Extended X-ray absorption fine structure (EXAFS) measurements were done at the Argonne National Laboratory Advanced Photon Source (APS) facility operating at 100 mA and 7.0 GeV at the Sector 5 BM-D hut. The LSCrPd samples, along with the standards  $\text{PdO}\cdot\text{H}_2\text{O}$  and Pd metal foil, were measured in transmission mode. The LSCrPd samples were in the form of pressed pellets 0.7 mm thick. The  $\text{PdO}\cdot\text{H}_2\text{O}$  standard was selected over PdO for convenience. The  $\text{PdO}\cdot\text{H}_2\text{O}$  standard was prepared by spreading a uniform layer of powder onto adhesive tape and measuring 16 stacked layers of tape. Each measurement included a Pd metal foil reference to calibrate the absorption edge energy, which was set to 24,350 eV for the foil. Both the samples and standards were measured from 200 eV below the edge to 750 eV above the Pd K edge ( $k = 14 \text{ \AA}^{-1}$ ). The  $\chi(k)$  spectra were extracted and Fourier transformed with a sine window over the region  $k = 2.3\text{--}10.9 \text{ \AA}^{-1}$  using the IFFEFIT program suite [14–18]. The Fourier transforms shown below are uncorrected for phase-shift.

### 3. Results and discussion

#### 3.1. Cell performance and stability

Fig. 1 shows a typical voltage versus time plot for an SOFC with an LSCrPd–GDC anode operated at 800 °C and a constant current density ( $J$ ) of  $0.6 \text{ A cm}^{-2}$ . The maximum cell potential (0.76 V)

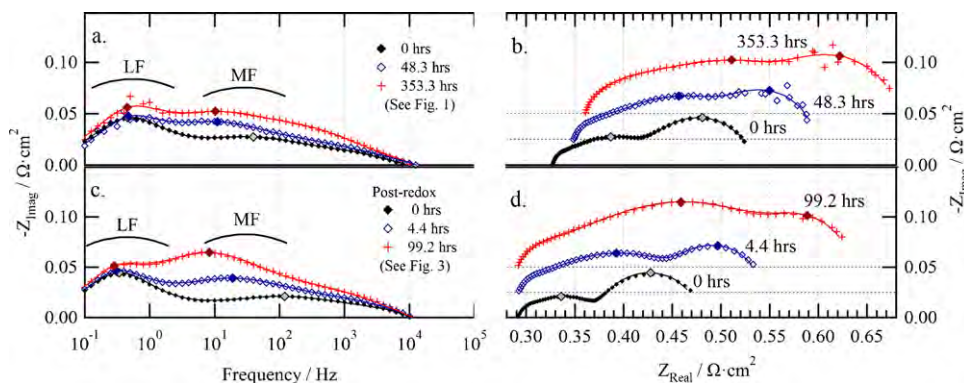


Fig. 2. Bode (a) and Nyquist plots (b) of the impedance spectra recorded at  $t = 0, 48.3,$  and  $353.3 \text{ h}$  during break-in of an LSCrPd–GDC cell. Bode (c) and Nyquist plots (d) recorded after a redox cycle at  $t = 0, 4.4$  and  $99.2 \text{ h}$ . Raw data are presented as symbols and the calculated fits to the spectra are presented as lines. The large diamonds mark the characteristic frequencies calculated from the fits.

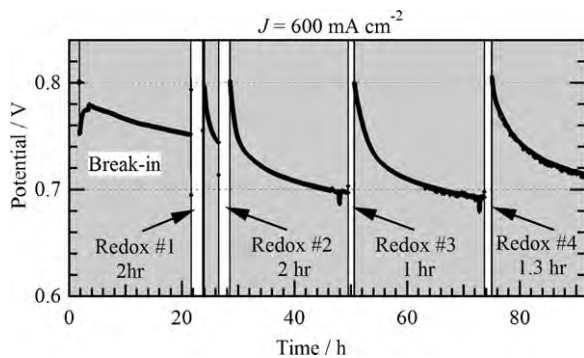
**Table 1**Performance summary for cells with anodes containing  $\text{La}_{0.8}\text{Sr}_{0.2}\text{Cr}_{0.8}\text{Pd}_{0.2}\text{O}_{3-\delta}$ ,  $\text{La}_{0.8}\text{Sr}_{0.2}\text{Cr}_{0.95}\text{Pd}_{0.05}\text{O}_{3-\delta}$ , and  $\text{La}_{0.8}\text{Sr}_{0.2}\text{CrO}_{3-\delta}$  [8,13].

Pd on B site (fraction)	Initial performance		Final performance		
	Power density at 0.7 V ( $\text{mW cm}^{-2}$ )	Initial $R_p$ ( $\Omega \text{ cm}^2$ )	Power density at 0.7 V ( $\text{mW cm}^{-2}$ )	Final $R_p$ ( $\Omega \text{ cm}^2$ )	Time elapsed (h)
0.2	508	0.22	390	0.33	353
0.05	380	0.38	280	0.44	180
0	80	1.53	180	0.72	312

was observed at the start of electrical testing, followed by continuous degradation at an average rate of  $1.4 \text{ mV h}^{-1}$  during the first 20 h. The degradation gradually slowed until the cell stabilized at 0.67 V after 200 h at a power density of  $390 \text{ mW cm}^{-2}$  at 0.7 V (Table 1). The cell open-circuit potential varied only slightly (<0.3%) during the life test, indicating that the voltage decrease was entirely due to changes in cell resistance. Other cells exhibited a similar behavior, although the voltage usually increased slightly during the first 1–3 h of cell testing, before beginning to decrease. For example, one cell reached a maximum voltage of 0.79 V at  $0.6 \text{ A cm}^{-2}$ , at  $\sim 1$  h and finally stabilized at 0.64 V after 350 h.

A cell with lower Pd content LSCrPd05–GDC anode showed a similar behavior, with an early peak voltage that decreased before stabilizing after 180 h at  $280 \text{ mW cm}^{-2}$  (at 0.7 V). Table 1 summarizes these results for the two different Pd content anodes, and compares them to results from a similar cell with an LSCr–GDC anode [8,13]. The LSCr–GDC anode performance improved during operation, but the power density at 0.7 V reached only  $180 \text{ mW cm}^{-2}$ . That is, cell performance clearly improved with increasing Pd content.

Fig. 2A and B shows Bode and Nyquist plots, respectively, of EIS data measured at  $t=0$ , 48, and 353 h for the cell shown in Fig. 1  $R_p$  increased from  $0.22 \Omega \text{ cm}^2$  to  $0.33 \Omega \text{ cm}^2$  during the test. The impedance response at low frequency (LF) remained essentially unchanged during testing. Fuel dilution experiments were used to probe the nature of this process. The LF response for humidified hydrogen diluted with Ar was larger than when He was the diluent, suggesting that it was related to gas phase diffusion. The magnitude of the broad response centered at 10–100 Hz (MF) increased with time, while its characteristic frequency decreased. These two polarization arcs were attributed almost entirely to the anode, as the cathode polarization resistance was found to be relatively small. That is, measurements on symmetric LSCF/LSCF–GDC/LSGM/LSCF–GDC/LSCF cells with cathodes identical to the present full cells yielded a polarization resistance of only  $0.02 \Omega \text{ cm}^2$ , with a characteristic frequency of  $\sim 1000$  Hz at  $800^\circ\text{C}$ . Finally, EIS measurements on the above-mentioned LSCrPd05–GDC anode cell yielded  $R_p$  values of  $0.38 \Omega \text{ cm}^2$  at  $t=0$  h and  $0.44 \Omega \text{ cm}^2$  at  $t=180$  h.

**Fig. 3.** Cell voltage versus time during initial break-in and during subsequent redox cycling of the LSCrPd–GDC anode.

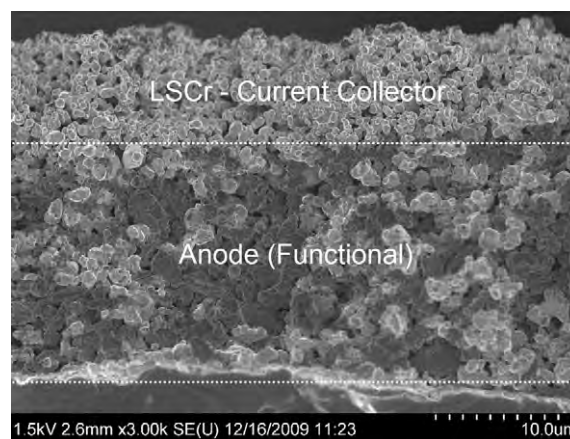
### 3.2. Redox behavior

Other cells were tested to evaluate the redox response of the anode. Fig. 3 shows an example where the cell was operated at steady state during the first 21 h. The maximum  $V$  of 0.78 V for this cell was reached after  $\sim 3$  h, after which  $V$  decreased at a rate similar to that shown in Fig. 1. The cell was then subjected to a number of anode redox cycles. After each redox cycle, the cell performance was substantially improved: the voltage measured at  $J=600 \text{ mA cm}^{-2}$  immediately increased to 0.8 V, slightly higher than the initial  $V$ , and then degraded at a rate faster than observed during the initial cell break-in. A shorter (18 min) air exposure (not displayed) produced the same effect as the longer (1–2 h) air exposures in Fig. 3. Impedance data recorded after a redox cycle are shown in Fig. 2C and D. Immediately after the redox cycle, the spectrum was nearly identical to that at the start of cell operation ( $t=0$  h in Fig. 2A). That is, the MF response, that had grown during cell break-in, was substantially decreased by the redox cycle. Following the redox cycle, the impedance again showed an increase in the MF response, albeit at a faster rate. In cases where a cell was operated for longer times after a redox cycle, the impedance response stabilized and became very similar to that observed for cells operated at steady state (Fig. 2A). In summary, the impedance data suggest that the same processes were responsible for the initial cell performance degradation and the post-redox degradation.

### 3.3. Structural and chemical characterization

#### 3.3.1. Anode microstructure

The anode microstructure for the LSCrPd cell operated for 353 h is displayed in Fig. 4. The dark contrast in the image corresponds to GDC and the light contrast to the chromite phases. The anode functional layer thickness was  $20 \mu\text{m}$  and the chromite current collector was  $10 \mu\text{m}$ . No cracking or delamination was observed in this or in larger-area images.

**Fig. 4.** Scanning electron micrograph of the LSCrPd–GDC anode after operation for 353 h in humidified  $\text{H}_2$  at  $800^\circ\text{C}$ .

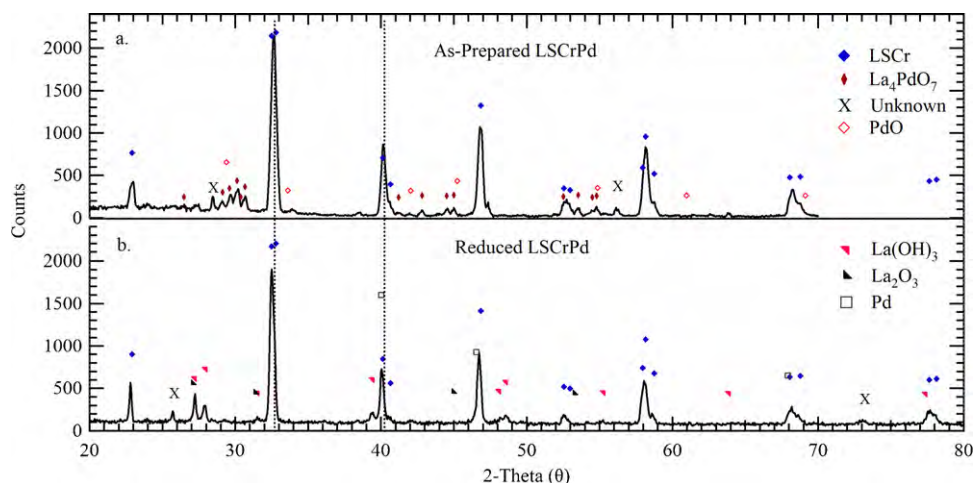


**Fig. 5.** The XRD patterns of (a) as-prepared LSCrPd powder and (b) reduced LSCrPd powder. The symbols show the angle and relative intensities of reflections for various relevant substances, from powder diffraction files.

### 3.3.2. X-ray powder diffraction

Structural studies of the anodes were carried out to explore the reasons for the performance break-in and regenerative behavior. Powder X-ray diffraction patterns of the as-prepared LSCrPd (Fig. 5A) powder closely matched the rhombohedral perovskite  $\text{La}_{0.85}\text{Sr}_{0.15}\text{CrO}_{3-\delta}$  [19], but several low intensity peaks were also detected that matched PdO and  $\text{La}_4\text{PdO}_7$  [20]. Analysis of the pattern using the relative intensity ratios of  $\text{La}_{0.85}\text{Sr}_{0.15}\text{CrO}_{3-\delta}$  and  $\text{La}_4\text{PdO}_7$  indicated that the mole fraction of  $\text{La}_4\text{PdO}_7$  was  $\sim 3\%$ . PdO was just above the detection limit. After reducing the as-prepared powder for 1 h at  $800^\circ\text{C}$  in humidified  $\text{H}_2$ , peaks matching  $\text{La}(\text{OH})_3$  were observed (Fig. 5B), consistent with reports that  $\text{La}_4\text{PdO}_7$  decomposes into Pd and  $\text{La}_2\text{O}_3$  in  $\text{H}_2$  at  $800^\circ\text{C}$  ( $\text{La}_2\text{O}_3$  rapidly transforms to  $\text{La}(\text{OH})_3$  at room temperature when exposed to lab air) [20,21]. It was not possible to determine if metallic Pd was present from the X-ray data, due to multiple peak overlaps with the perovskite pattern. However, in one TEM image from the as-prepared material, a single,  $\sim 1$ -micron-diameter metallic Pd particle was observed.

### 3.3.3. EXAFS

Fig. 6 shows the Fourier transform of the EXAFS, uncorrected for phase shift, from both the as-prepared (oxidized) and the reduced LSCrPd. For the as-prepared material, a broad peak at  $\sim 1.5$ – $2\text{ \AA}$  overlapped peaks from both the PdO·xH<sub>2</sub>O standard (at  $1.5\text{ \AA}$ ) and

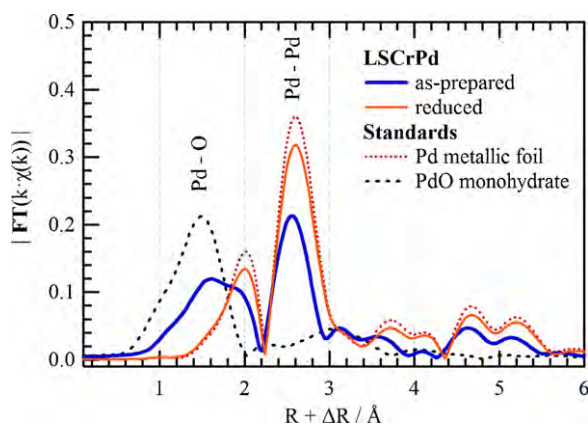


**Fig. 6.** The Fourier transform of the EXAFS for the as-prepared and reduced LSCrPd powder samples and Pd metal and PdO·H<sub>2</sub>O standards.

the Pd standard (at  $2.6\text{ \AA}$ ), indicating that both oxidized and metallic Pd were present. This suggests that metallic Pd was present during firing in air – not surprising given that PdO decomposes above  $800^\circ\text{C}$  – and that it was retained even during cooling below  $800^\circ\text{C}$  where PdO is stable [22]. This would occur if large metallic Pd particles were present during high-temperature firing but did not fully oxidize during cooling, consistent with the above TEM observation. The EXAFS of the reduced LSCrPd sample showed peaks exclusive to metallic Pd, indicating that all of the Pd in the sample was in the metallic state.

Although the LSCrPd powder was not phase pure, the relatively small amounts of metallic Pd and  $\text{La}_4\text{PdO}_7$  (or  $\text{La}_2\text{O}_3$  and Pd after reduction) were unlikely to have a strong impact on electrochemical performance, especially as they were relatively large particles with low surface area. This interpretation is supported by the LSCrPd05 anode results; these showed a similar electrochemical behavior as the LSCrPd, but were much closer to being phase pure.

### 3.3.4. STEM

Fig. 7 shows STEM images from LSCrPd powders at various stages. The as-prepared powder showed perovskite oxide particles (Fig. 7A) that contained Pd near the detection limit ( $\sim 1\%$ ) of STEM-EDS. After reduction for 1 h in humidified  $\text{H}_2$  (Fig. 7B), the perovskite surfaces were decorated with nano-particles with an average diameter of 8 nm. STEM-EDS line scans indicated that these nano-particles were Pd-rich, and most likely Pd metal. The nano-particles presumably formed by precipitation from the perovskite particle, and provide clear evidence that Pd was present in the perovskite phase prior to reduction. The observation of nano-particles explains the initial voltage increase ( $R_p$  decrease) at the onset of cell testing, analogous to results for Ru- and Ni-substituted chomite anodes where metallic nano-particles decreased  $R_p$  [9]. The subsequent voltage decrease in Figs. 1 and 3 is likely explained by coarsening of Pd nano-particles, again analogous to prior reports for Ni- and Ru-substituted chomites [7,9]. However, the Pd nucleation and degradation processes occurred faster than for the Ru-substituted chromite, where minimum  $R_p$  was reached after  $>50\text{ h}$  and there was only a few % degradation after 300 h at  $800^\circ\text{C}$  [7]. This may be due to the much lower melting point of Pd compared to Ru, which should promote faster diffusion kinetics.

Subsequent exposure of the reduced powder to air essentially eliminated the Pd nano-particles (Fig. 7C), suggesting that the Pd

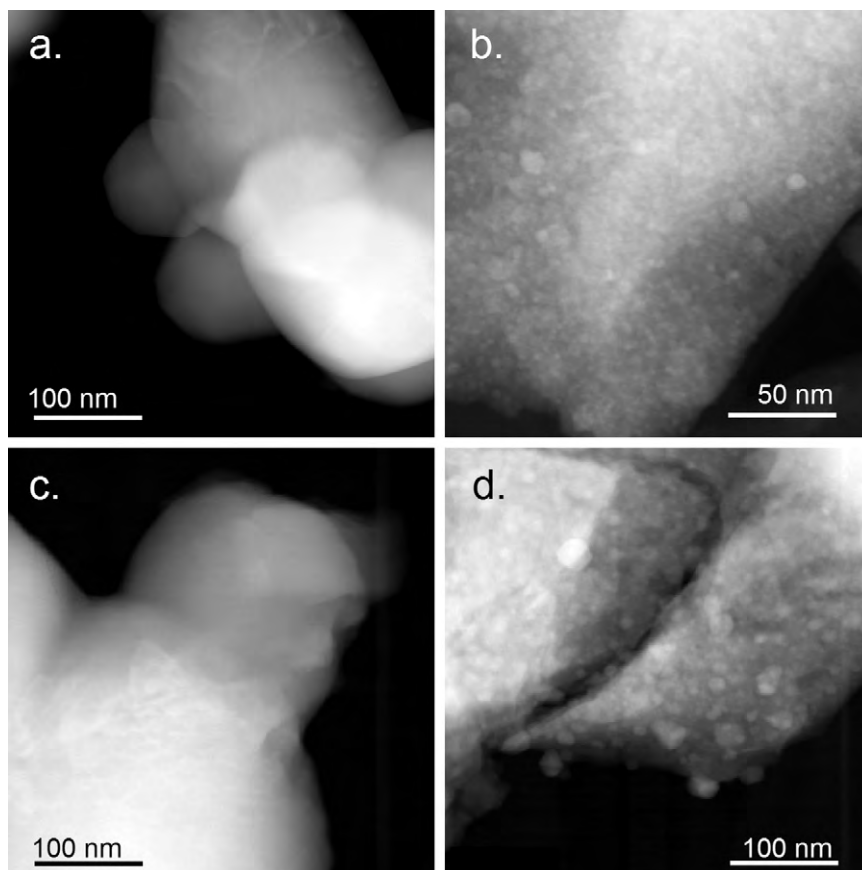


**Fig. 7.** STEM micrographs of LSCrPd (a) as-prepared powder, (b) powder reduced for 1 h at 800 °C, (c) powder reduced for 27 h at 800 °C and then exposed to air for 1 h at 800 °C, and (d) the powder from (c) reduced for 12 h at 800 °C.

had either re-dissolved into the perovskite or formed an oxide that uniformly coated the particle surface. Finally, Fig. 7D shows that re-reduction of the powder for 12 h resulted in the re-nucleation of Pd nano-particles, explaining the recovery of cell performance in Fig. 3 and the decrease in polarization resistance in Fig. 2C and D. The maximum voltage and subsequent degradation both occurred more quickly after the redox cycles compared to the initial anode operation (Figs. 1 and 2). This may indicate that Pd remained near the perovskite particle surface during the oxidation. Thus, the diffusion distance for Pd to reach the surface and cause Pd particle growth was less than in the initial perovskite particles, where the Pd was presumably uniformly distributed.

#### 4. Summary and conclusions

SOFCs with LSCrPd–GDC anodes were tested at 800 °C in humidified H<sub>2</sub>. Cells exhibited a break-in during which performance peaked and then degraded before stabilizing. The structural evidence suggests that the good initial performance was due to the nucleation of Pd nano-particles on chromite particle surfaces upon reduction. After stabilization, these anodes provide steady-state performance similar to other oxide-based anodes [7,8,10,13].

On the other hand, these anodes possess a unique new feature—the original low resistance can be regenerated repeatedly by performing anode redox cycles. The performance improvement is attributed to the observed elimination of the Pd nano-particles upon oxidation, and nano-particle re-nucleation upon subsequent reduction. The ability to return nano-scale anodes to their initial low resistance after degradation could be important given their tendency to lose activity due to coarsening [7]. In intermittent SOFC applications [23,24], for example, it would be possible to expose

the hot anodes to air during shut down, in order to regenerate them for the subsequent operational cycle. The present results at 800 °C show a quite rapid resistance increase after regeneration, perhaps too fast even for an intermittent application. However, future studies may show ways to improve stability. For example, preliminary results with these anodes show that the degradation rate decreases with decreasing operating temperature.

#### Acknowledgments

The authors gratefully acknowledge financial support from the Department of Energy (Award No. DE-FG02-05ER46255). EPN also acknowledges support from the National Science Foundation RET program, while DMB and SAB acknowledge support from the Petroleum Research Fund and NSF grant CBET-0854223. The EXAFS measurements were performed at the Du-Pont-Northwestern-Dow Collaborative Access Team (DND-CAT) located at Sector 5 of the APS. DND-CAT is supported by E.I. Dupont de Nemours & Co., The Dow Chemical Company and the State of Illinois. Use of the APS was supported by the US Department of Energy, Office of Science, Office of Basic Energy Sciences, under Contract No. DE-AC02-06CH11357. DMB and CAH thank Dr. Qing Ma for assistance with the EXAFS measurements.

#### References

- [1] A. Atkinson, S. Barnett, R.J. Gorte, J.T.S. Irvine, A.J. McEvoy, M. Mogensen, S.C. Singhal, J. Vohs, *Nat. Mater.* 3 (2004) 17–27.
- [2] Y.H. Huang, R.I. Dass, Z.L. Xing, J.B. Goodenough, *Science* 312 (2006) 254–257.
- [3] S.W. Tao, J.T.S. Irvine, *Nat. Mater.* 2 (2003) 320–323.
- [4] J.M. Haag, B.D. Madsen, S.A. Barnett, K.R. Poeppelmeier, *Electrochem. Solid-State Lett.* 11 (2008) B51–B53.

- [5] M.D. Gross, J.M. Vohs, R.J. Gorte, *Electrochem. Solid-State Lett.* 10 (2007) B65–B69.
- [6] X.C. Lu, J.H. Zhu, Z. Yang, G. Xia, J.W. Stevenson, *J. Power Sources* 192 (2009) 381–384.
- [7] B.D. Madsen, W. Kobsiriphat, Y. Wang, L.D. Marks, S.A. Barnett, *J. Power Sources* 166 (2007) 64–67.
- [8] W. Kobsiriphat, Ceramic anode materials with nanoscale electrocatalysts for solid oxide fuel cells, Ph.D. Thesis, Department of Materials Science and Engineering, Northwestern University (2007).
- [9] B.D. Madsen, W. Kobsiriphat, Y. Wang, L.D. Marks, S. Barnett, *ECS Trans.* 7 (2007) 1339–1348.
- [10] W. Kobsiriphat, B.D. Madsen, Y. Wang, M. Shah, L.D. Marks, S.A. Barnett, *J. Electrochem. Soc.* 157 (2010) B279–B284.
- [11] H. Fukunaga, Y. Numazawa, A. Fueoka, C. Arai, T. Takatsuka, K. Yamada, *J. Chem. Eng. Jpn.* 40 (2007) 1183–1186.
- [12] Y. Nishihata, J. Mizuki, H. Tanaka, M. Uenishi, M. Kimura, *J. Phys. Chem. Solids* 66 (2005) 274–282.
- [13] W. Kobsiriphat, B.D. Madsen, Y. Wang, L.D. Marks, S.A. Barnett, *Solid State Ionics* 180 (2009) 257–264.
- [14] M. Newville, P. Livins, Y. Yacoby, J.J. Rehr, E.A. Stern, *Jpn. J. Appl. Phys.* 32 (1993) 125–127.
- [15] B. Ravel, M. Newville, J.O. Cross, C.E. Bouldin, *Physica B* 208 (1995) 145–147.
- [16] B. Ravel, M. Newville, *J. Synchron. Radiat.* 12 (2005) 537–541.
- [17] M. Newville, *J. Synchron. Radiat.* 8 (2001) 322–324.
- [18] M. Newville, *J. Synchron. Radiat.* 8 (2001) 96–100.
- [19] K. Tezuka, Y. Hinatsu, A. Nakamura, T. Inami, Y. Shimojo, Y. Morii, *J. Solid State Chem.* 141 (1998) 404–410.
- [20] M. Andersson, J. Grins, M. Nygren, *J. Solid State Chem.* 146 (1999) 428–436.
- [21] M. Andersson, K. Jansson, M. Nygren, *Catal. Lett.* 39 (1996) 253–259.
- [22] H. Zhang, J. Gromek, G. Fernando, H. Marcus, S. Boorse, *J. Phase Equil.* 23 (2002) 246–248.
- [23] J.L. Martin, P. Osenar, *ECS Trans.* 25 (2009) 249–257.
- [24] N. Minh, A. Anumakonda, R. Doshi, J. Guan, S. Huss, G. Lear, K. Montgomery, E. Ong, J. Yamanis, *ECS Trans.* 16 (2001) 190–195.